Weierstraß-Institut
für Angewandte Analysis und Stochastik
Leibniz-Institut im Forschungsverbund Berlin e. V.

Preprint ISSN 0946 – 8633

Multiscale modeling of weakly compressible elastic materials in harmonic regime and applications to microscale structure estimation

Alfonso Caiazzo[1], Joaquín Mura[2]

submitted: May 22, 2013

[1] Weierstrass Institute
Mohrenstr. 39
10117 Berlin
Germany
E-Mail: Alfonso.Caiazzo@wias-berlin.de

[2] Civil Engineering School
Pontificia Universidad Católica de Valparaíso
Av. Brasil 2147, Valparaíso
Chile
E-Mail: joaquin.mura@ucv.cl

No. 1786
Berlin 2013

2010 *Mathematics Subject Classification.* 65Z05, 74Q05, 74Q15, 92-08.

Key words and phrases. Homogenization, linear elasticity, weakly compressible material, inverse problem, elastography.

Edited by
Weierstraß-Institut für Angewandte Analysis und Stochastik (WIAS)
Leibniz-Institut im Forschungsverbund Berlin e. V.
Mohrenstraße 39
10117 Berlin
Germany

Fax: +49 30 20372-303
E-Mail: preprint@wias-berlin.de
World Wide Web: http://www.wias-berlin.de/

Abstract

This article is devoted to the modeling of elastic materials composed by an incompressible elastic matrix and small compressible gaseous inclusions, under a time harmonic excitation. In a biomedical context, this model describes the dynamics of a biological tissue (e.g. lung or liver) when wave analysis methods (such as Magnetic Resonance Elastography) are used to estimate tissue properties. Due to the multiscale nature of the problem, direct numerical simulations are prohibitive. We extend the homogenized model introduced in [Baffico, Grandmont, Maday, Osses, *SIAM J. Mult. Mod. Sim.*, **7**(1), 2008] to a time harmonic regime to describe the solid-gas mixture from a macroscopic point of view in terms of an effective elasticity tensor. Furthermore, we derive and validate numerically analytical approximations for the effective elastic coefficients in terms of macroscopic parameters. This simplified description is used to to set up an efficient variational approach for the estimation of the tissue porosity, using the mechanical response to external harmonic excitations.

1 Introduction

Computational modeling of biological tissues is a complex multiscale problem, involving the interaction of various physical phenomena across multiple scales. Since in clinical applications the tissues are generally viewed as continuum materials, an important issue from the point of view of mathematical and numerical models is the characterization of the non trivial contributions of microscopic physical and geometrical to the overall behavior, especially in terms of compressibility and effective elasticity. These aspect is of utmost importance in a biomedical context, as detecting tissue inhomogeneities is a crucial step in the diagnosis process.

Nowadays, non-invasive imaging techniques became a very important tool in biomedical research, as they allow detailed insights into the properties of living organisms. Magnetic Resonance Elastography (MRE) is a recently developed quantitative imaging technique, which is used to estimate structural properties of soft tissues [19]. In MRE experiments, the tissue undergoes external harmonic excitations, as shear or compression waves, and Magnetic Resonance Imaging (MRI) is then used to measure the mechanical response, in terms of the internal displacement map (e.g. [25]) and the divergence field [14]. This procedure is used in clinical research for *in vivo* and *in vitro* studies of biological tissues (such as brain and lungs) to obtain stiffness and compressibility information, predicting and localizing tissue anomalies (see, e.g., [11, 25, 29]). In order to reconstruct these tissue properties from MRE data, current research has achieved valuable numerical modeling approaches. In particular, variational-based approaches for inverse problems have been successfully applied for the estimation of shear modulus in the linear elastic regime [3, 15, 21, 22], for viscoelastic tissues [17], and recently extended to poroelastic models [16, 20]. Besides the estimation of mechanical properties, in some

cases also geometrical microstructure information can be recovered, by analyzing directly the MR images (see, e.g., [14, 24]). However, up to our knowledge, the problem of automatically estimating microscale properties via MRE data has not been addressed in detail.

The goal of this work is to develop an effective model for the simulation of weakly compressible materials, which, through an up-scaling of the smallest spatial scales can be effectively used to solve the inverse problem of estimating material porosity starting from MRE experiments. Similarly to [12, 13], by considering the effect of very fine mixtures in the macroscopic scale, we adopt a variational approach to construct a sequence for the detection and location of regions with different porosity through the solution of an adjoint problem. The solution of inverse problems typically requires solving multiple times the forward problem. Hence, the cost of a full microscale simulation might become a bottleneck for the overall efficiency. Recently, several model order reduction techniques have been proposed in combination with inverse problems in biomedical context, e.g. for cardiac electromechanics [8], shape optimization in hemodynamic [1, 2] and for data assimilation in computational elasticity [18]. In this work, we address this issue reducing the complexity of the forward problem by deriving a simplified description of the material microscale from a macroscale point of view.

We model the weakly compressible tissue as an elastic materials composed of of a very fine mixture of an *incompressible* elastic matrix and *compressible* gaseous inclusions. Moreover, we restrict to the case of non-connected gaseous compartments. This approximation can provide an idea of the effective elastic properties of the tissue, which are important when considering the propagation of mechanical stimuli [7], such as harmonic pressure waves. Our two-scale approach is based on a recently proposed homogenization procedure to derive effective material equations for the matrix–gas mixture in a static regime [7]. In this approach, the small inhomogeneities are upscaled into the larger scale using the homogenization theory (see e.g. [4, 5, 28]), where the microscopic model is transformed into a macroscopic model in the weak limit when the size of the inhomogeneities goes to zero.

In this contribution we formally extend the results of [7] to a time harmonic regime. Moreover, we explicitly validate the multiscale model against a direct numerical simulation at the microscale level. As a further result, combining theoretical considerations and numerical observations, we obtain a approximated analitical expression for the effective elasticity tensor of the homogenized gas–matrix mixture, parametrizing the multiscale model using only gas pressure, tissue elasticity and material porosity.

Through the analytical parameterization, we set up a minimization procedure with the porosity as an optimization parameter. In particular, since the MRE may provide measurement of interior displacement field from a given specimen, this type of data will be considered to define the cost functional to be minimized. As a result, we demonstrate that through the homogenization of the smaller scale, we are able to estimate the material porosity – a quantity related to the microscale – using macroscale computations only. We validate the algorithm considering synthetic data, obtained perturbing the results of direct numerical simulations at the microscale level.

The rest of the paper is organized as follows. In Section 2 we describe the two-scale homogenization, extending the results of [7] to the harmonic regime. In Section 3 we derive semi-analytical expressions of the effective tensor coefficients, validating the results for a wide range of physical parameters. These results are used in Section 4 to define a multiscale variational

inverse problem for the estimation of porosity starting from measurement of the internal displacement field. Finally, Section 5 draws the conclusions.

2 Modeling of incompressible elastic materials with gaseous inclusions

In what follows, we will assume to deal with an elastic material, composed by an incompressible matrix, with elasticity modulus μ and small gaseous inclusions of different sizes. Furthermore, let p_a be the environmental gas pressure. For the development of the multiscale model we will assume that:

(A.i) the gaseous inclusions are very small with respect to the matrix and isolated from each other,

(A.ii) they can be organized into a periodic array,

(A.iii) they have almost the same shape.

Within these hypotheses, the effective material properties can be obtained via a two-scale homogenization approach, in order to characterize the effect of microscale geometry (i.e. the gaseous inclusions) only from a macroscopic point of view [26, 27].

Some recently proposed approaches concerning homogenization in the context of elasticity problems can be found e.g. in [6, 10]. We adopt the two scales homogenization presented in [7], which is summarized in this section, discussing the extension of the formulations to a time harmonic regime.

2.1 Two-scale asymptotic in harmonic regime

Let a bounded domain $\Omega \subset \mathbb{R}^d$ ($d = 2, 3$) represent the compressible material, composed of an incompressible matrix and several small gaseous inclusion of spherical shape. Furthermore, let the small parameter $0 < \epsilon \ll 1$, denote the aspect ratio between the inclusions and the container matrix. Under the above assumptions (A.i)–(A.iii), we consider the composite material as the combination of a finite (but large) number of equal *microscopic* cells

$$\Omega = \bigcup_i \Omega_{\epsilon,i}$$

where $\Omega_{\epsilon,i} := \epsilon Y + \mathbf{x}_i$ contain a single inlcusion, $Y = [0, 1]^N$ is the unitary cell in $\mathbb{R}^N$ ($N = 2, 3$), and $\mathbf{x}_i$ denotes the center of the cell (see Figure 2.1). In this configuration, the unitary cell Y can be decomposed as

$$Y = Y_S \cup \Gamma \cup Y_F$$

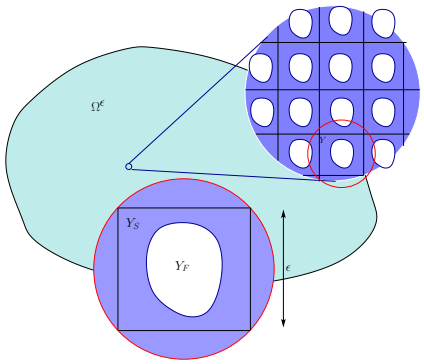

Figure 1: Sketch of the microscopic and macroscopic scales in the composite material.

where Y_S and Y_F stand for the domains occupied by the solid and by the gaseous part, respectively, while Γ denotes the interface between them (as shown in Figure 2.1). The incompressible elastic matrix, which will be denoted by Ω^ϵ, consists of the union of all the solid subdomains of the microscopic cells.

In what follows, we will restrict to the case of spherical inclusions, referring to them as *bubbles*.

Remark 2.1 (Porosity) *Since it is assumed that the gas is confined within a volume $\epsilon|Y_F|$ and it is embedded into a unit cell of volume $\epsilon|Y|$, after scaling, the* porosity *of the material, defined as the fraction of volume occupied by the gas, is given by*

$$\phi = |Y_F| \, .$$

Remark 2.2 (Effective density) *Let $\chi^{k,\epsilon}(y)$ denote the characteristic function of the solid domain in the cell k.If the solid matrix has a constant density ρ_S, then the effective density in the microscopic cell is given by*

$$\rho_\epsilon(y) = \sum_k \rho_S \chi_S^{k,\epsilon}(y)$$

(summing up all the contribution of the cells), while the cell-averaged density is

$$\overline{\rho} = \frac{1}{|Y|} \int_Y \rho_\epsilon(y) \, dy = \frac{|Y_S|}{|Y|} \rho_S = (1-\phi)\rho_S \, . \tag{1}$$

2.1.1 Linear elasticity equations

We assume that the bubbles are filled by a perfect gas, initially at equilibrium. Since the bubbles are small and isolated, the relationship between the external pressure, denoted by p_a (which is also the average one at each bubble), and the pressure variation in the k-th cell can be computed as [9, pag. 83]

$$\delta p_\epsilon^k = p_\epsilon^k - p_a \approx \frac{A}{\epsilon^N} \left(\int_{\Gamma^{\epsilon,k}} \mathbf{d}^\epsilon \cdot n^\epsilon \, ds \right) \tag{2}$$

where $\Gamma^{\epsilon,k}$ denotes the boundary of the gaseous inclusion and

$$A = \frac{p_a}{N\phi} \tag{3}$$

(linearizing the perfect gas law around the equilibrium state).

We focus on a time harmonic dynamics driven by a periodic external forcing with a given frequency ω. Since the frequency is fixed, i.e. it does not depend on ϵ, ω must be considered not very high, so that the associated wavelength is not comparable with the pore size. In the linear elastic regime, in the frequency space, the displacement field $\mathbf{d}^\epsilon$ and the gas pressure q^ϵ of the medium are described by the following elasticity equation:

$$\left\{\begin{array}{rcll} -\overline{\rho}\omega^2\mathbf{d}^\epsilon - \operatorname{div}\sigma(\mathbf{d}^\epsilon, q^\epsilon) &=& 0 & \text{in } \Omega^\epsilon, \\ \operatorname{div}(\mathbf{d}^\epsilon) &=& 0 & \text{in } \Omega^\epsilon, \\ \sigma(\mathbf{d}^\epsilon, q^\epsilon)n^\epsilon + \dfrac{A}{\epsilon^N}\left(\displaystyle\int_{\Gamma^{\epsilon,k}} \mathbf{d}^\epsilon \cdot n^\epsilon \, ds\right)\boldsymbol{n}^\epsilon &=& 0 & \text{on } \Gamma^{\epsilon,k},\ k = 1, \ldots \\ \mathbf{d}^\epsilon &=& \mathbf{d}_{ext} & \text{on } \Gamma_N, \\ \mathbf{d}^\epsilon \cdot \boldsymbol{n}^\epsilon &=& 0 & \text{on } \Gamma_D. \end{array}\right. \tag{4}$$

together with the constitutive relation

$$\sigma(\mathbf{d}^\epsilon, q^\epsilon) = 2\mu e(\mathbf{d}^\epsilon) - q^\epsilon I,$$

where $e(\mathbf{d}) = 1/2\left(\nabla\mathbf{d} + \nabla\mathbf{d}^T\right)$ stands for the linear strain tensor. In (4), the subsets Γ_N and Γ_D of the $\partial\Omega^\epsilon$ denotes the external Neumann and the Dirichlet boundaries, respectively.

2.1.2 Asymptotic expansion

In order to obtain the effective equations in the limit $\epsilon \to 0$ of small bubbles, we introduce the multiscale ansatzs

$$\mathbf{d}^\epsilon(x) = \mathbf{d}^0(x, x/\epsilon) + \epsilon\mathbf{d}^1(x, x/\epsilon) + \epsilon^2\mathbf{d}^2(x, x/\epsilon) + O(\epsilon^3) \tag{5}$$

for the displacement, and

$$q^\epsilon(x) = \epsilon^{-1}q^{-1}(x, x/\epsilon) + q^0(x, x/\epsilon) + \epsilon q^1(x, x/\epsilon) + O(\epsilon^2) \tag{6}$$

for the pressure. Furthermore, we denote with $y = x/\epsilon$ the so-called *fast variable* (defined in the unit cell Y), splitting the spatial derivative as

$$\partial = \partial_x + (1/\epsilon)\partial_y\,. \tag{7}$$

Using (5) and (7), the incompressibility condition $(4)_2$ reads, at the leading order,

$$\operatorname{div}_y(\mathbf{d}^0) = 0 \quad \text{in } Y_S\,, \tag{8}$$

while, at the order $O(\epsilon^j)$, $j > 0$, we get

$$\operatorname{div}_x(\mathbf{d}^{j-1}) + \operatorname{div}_y(\mathbf{d}^j) = 0, \quad \text{in } Y_S. \tag{9}$$

Inserting these expressions into $(4)_1$, and using (5)–(7) yields

$$\text{order } \epsilon^{-2}\text{: } 2\mu \operatorname{div}_y(e_y(\mathbf{d}^0)) - \nabla_y q^{-1} = \operatorname{div}_y \sigma_y(\mathbf{d}^0, q^{-1}) = 0 \tag{10}$$

$$\epsilon^{-1}\text{: } 2\mu \left(\operatorname{div}_y(e_y(\mathbf{d}^1)) + \operatorname{div}_x(e_y(\mathbf{d}^0)) + \operatorname{div}_y(e_x(\mathbf{d}^0))\right) - \nabla_x q^{-1} - \nabla_y q^0 = 0 \tag{11}$$

$$\epsilon^{0}\text{: } \overline{\rho}\omega^2 \mathbf{d}^0 + 2\mu \left(\operatorname{div}_x(e_x(\mathbf{d}^0)) + \operatorname{div}_x(e_y(\mathbf{d}^1))\right) + 2\mu \left(\operatorname{div}_y(e_x(\mathbf{d}^1)) + \operatorname{div}_y(e_y(\mathbf{d}^2))\right) - \nabla_x q^0 - \nabla_y q^1 = 0 \tag{12}$$

$$\epsilon^{1}\text{: } \overline{\rho}\omega^2 \mathbf{d}^1 + 2\mu \left(\operatorname{div}_x(e_x(\mathbf{d}^1)) + \operatorname{div}_x(e_y(\mathbf{d}^2)) + \operatorname{div}_y(e_x(\mathbf{d}^2))\right) - \nabla_x q^1 + E(\mathbf{d}^3, q^2) \tag{13}$$

where $E(\mathbf{d}^3, q^2)$ is an $O(1)$ residual term depending on the third order displacement and second order pressure.

From (8)–(13), one obtains the system of equations for the unit cell Y, describing the dynamics at the bubble scale, at different order in ϵ. For the leading order we have

$$\left\{\begin{array}{rcll} -\operatorname{div}_y \sigma_y(\mathbf{d}^0, q^{-1}) &=& 0 & \text{in } \Omega \times Y_S, \\ \operatorname{div}_y(\mathbf{d}^0) &=& 0 & \text{in } \Omega \times Y_S, \\ \sigma_y(\mathbf{d}^0, q^{-1})\boldsymbol{n} &=& 0 & \text{on } \Omega \times \Gamma, \\ \mathbf{d}^0 \text{ and } q^{-1} & & Y-\text{periodic} & \end{array}\right. \tag{14}$$

whose solution is given by a displacement field $\mathbf{d}^0$ and a pressure q^{-1} constant in y (but not in x). For the first order in ϵ, collecting the other terms for $\mathbf{d}^1$ and q^0 yields

$$\left\{\begin{array}{rcll} -\operatorname{div}_y \sigma_y(\mathbf{d}^1, q^0) &=& 0 & \text{in } \Omega \times Y_S, \\ \operatorname{div}_y \mathbf{d}^1 &=& -\operatorname{div}_x \mathbf{d}^0 & \text{in } \Omega \times Y_S, \\ \sigma_y(\mathbf{d}^1, q^0)n &=& -2\mu e_x(\mathbf{d}^0)n + A|Y| \operatorname{div}_x \mathbf{d}^0\, n & \text{on } \Omega \times \Gamma. \\ \mathbf{d}^1 \text{ and } q^0 & & Y-\text{periodic} & \end{array}\right. \tag{15}$$

The second order is described by

$$\left\{\begin{array}{rcll} -\operatorname{div}_y \sigma_y(\mathbf{d}^2, q^1) &=& \overline{\rho}\omega^2 \mathbf{d}^0 + \operatorname{div}_x(\sigma_y(\mathbf{d}^1, q^0) + \sigma_x(\mathbf{d}^0, 0)) + \operatorname{div}_y \sigma_x(\mathbf{d}^1, 0) & \text{in } Y_S, \\ \operatorname{div}_y(\mathbf{d}^2) &=& -\operatorname{div}_x(\mathbf{d}^1) & \text{in } Y_S, \\ \sigma_y(\mathbf{d}^1, q^0)n &=& -\sigma_x(\mathbf{d}^1, 0)n + A\left(\displaystyle\int_Y \operatorname{div}_x(\mathbf{d}^1)dy - |Y| y \cdot \nabla_x \operatorname{div}_x(\mathbf{d}^0)\right)\boldsymbol{n} & \\ & & +A\left(|Y_F| y \cdot \nabla_x(\operatorname{div}_x(\mathbf{d}^0) + \operatorname{div}_y(\mathbf{d}^1))dy\right)\boldsymbol{n} & \text{on } \Gamma, \\ & & \mathbf{d}^2 \text{ and } q^1\, Y-\text{periodic} & \end{array}\right. \tag{16}$$

Notice that, since the frequency is independent from ϵ, the equations (14), (15) and (16) do not depend on the harmonic waves. In other words, at the spatial scale of the bubbles, the length-wave of the excitation is, at first order in ϵ, too large to be perceived with the fast variable y. The only contribution of the term associated with the frequency just appear in the right hand side of (16). This equation will be used later to obtain the formula of the effective tensor.

2.1.3 Homogenized elasticity tensor

For the large scale dynamics, using the recurrence for incompressibility relations (9), one obtains

$$\int_{Y_F} \operatorname{div}_y \mathbf{d}^1(x,z)dz = -\int_\Gamma \mathbf{d}^1 \cdot \boldsymbol{n} ds = -\int_{Y_S} \operatorname{div}_y \mathbf{d}^1(x,z)dz = |Y_S|(\operatorname{div}_x \mathbf{d}^0)(x),$$

i.e.

$$(\operatorname{div}_x \mathbf{d}^0)(x) = -\frac{1}{Y_S}\int_\Gamma \mathbf{d}^1 \cdot \boldsymbol{n} ds. \tag{17}$$

Furthermore, the compatibility condition in (16) yields

$$\begin{aligned} -\omega^2 \mathbf{d}^0 - \operatorname{div}_x(2\mu e_x(\mathbf{d}^0) - \frac{A|Y||Y_F|}{|Y_S|}\nabla_x \operatorname{div}_x(\mathbf{d}^0)) = \\ = \operatorname{div}_x\left(\frac{1}{|Y_S|}\int_{Y_S} \sigma_y(\mathbf{d}^1, q^0)(z)dz\right). \end{aligned} \tag{18}$$

Equation (18), can be rewritten as a differential problem for the macroscopic variable $\mathbf{d}^0$:

$$\begin{cases} -\overline{\rho}\omega^2 \mathbf{d}^0 - \operatorname{div}_x C^{eff} e_x(\mathbf{d}^0) &= 0 \quad \text{in } \Omega, \\ \mathbf{d}^0 &= \mathbf{d}_{ext} \quad \text{on } \Gamma_N, \\ \mathbf{d}^0 \cdot \boldsymbol{n} &= 0 \quad \text{on } \Gamma_D, \end{cases} \tag{19}$$

depending on the microstructure description $(\mathbf{d}^1, q^0)$, through an *effective elasticity tensor*

$$C^{eff}(\mathbf{d}^0) = \frac{p_a}{N(1-\phi)}\left(\operatorname{div}_x \mathbf{d}^0\right)\mathbf{I} + 2\mu e_x(\mathbf{d}^0) + \langle \sigma_y(\mathbf{d}^1, q^0)\rangle_{Y_S}. \tag{20}$$

The operator $\langle\cdot\rangle_{Y_S}$, introduced in (20), denotes the average operator in the solid part of the unit cell. The effective tensor (20) still depends on the microscopic variables $\mathbf{d}^1$ and q^0 which, at the same time, depend on $\mathbf{d}^0$. In order to overcome this problem, we consider the following change of variable [7]

$$\mathbf{d}^1(x,y) = \sum_{k,l=1}^N [e_x(\mathbf{d}^0)]_{kl}\chi^{kl},\ q^0(x,y) = \sum_{k,l=1}^N [e_x(\mathbf{d}^0)]_{kl}\eta^{kl}, \tag{21}$$

yielding

$$\left[\sigma(\mathbf{d}^1, q^0)\right]_{ij} = \sum_{k,l=1}^N \left[e_x(\mathbf{d}^0)\right]_{kl}\left[\sigma_y(\chi^{kl}, \eta^{kl})\right]_{ij}.$$

In terms of these new variables, we can write

$$C^{eff} e_x(\mathbf{d}^0) = (2\mu \mathbb{1} + \langle[\sigma_y(\chi,\eta)]\rangle_{Y_S})\, e_x(\mathbf{d}^0) + \frac{p_a}{N(1-\phi)}(\operatorname{div}_x \mathbf{d}^0)\mathbf{I},$$

which allows to rewrite the entries of the tensor C^{eff} as

$$C^{eff}_{ijkl} = \frac{p_a}{N(1-\phi)}\delta_{ij}\delta_{kl} + 2\mu\delta_{ijkl} + \langle[\sigma_y(\chi^{kl}, \eta^{kl})]_{ij}\rangle_{Y_S}, \tag{22}$$

with $\delta_{ijkl} := \frac{1}{2}(\delta_{li}\delta_{kj} + \delta_{ki}\delta_{lj})$. For convenience of notation, we define the following quantity associated to the microstructure:

$$\sigma_{ijkl} := \langle [\sigma_y(\chi^{kl}, \eta^{kl})]_{ij} \rangle_{Y_S} = \frac{1}{Y_S} \int_{Y_S} [\sigma_y(\chi^{kl}, \eta^{kl})(y)]_{ij} dy. \tag{23}$$

Remark 2.3 (Effective compressibility) *Equation* (22) *shows that the effective material is actually compressible, and that the effective Lamé's coefficients depends on p_a, on μ and on the microstructure dynamics, through the term σ_{ijkl}.*

Differential equations for the new set of variables χ^{kl} and η^{kl} can be obtained by replacing (21) into (19), yielding an auxiliary cell problem for the microstructure only [7]:

$$\begin{cases} -\operatorname{div}_y \sigma_y(\chi^{kl}, \eta^{kl}) &= 0 & \text{in } Y_S, \\ \operatorname{div}_y \chi^{kl} &= -\delta_{kl} & \text{in } Y_S, \\ \sigma_y(\chi^{kl}, \eta^{kl})\boldsymbol{n} &= -T^{kl} e_y(s^{kl})\boldsymbol{n} & \text{on } \Gamma, \\ \chi^{kl}, \eta^{kl} & \text{are } Y - \text{periodic.} \end{cases} \tag{24}$$

where the local tensor T^{kl} is defined by

$$T^{kl}_{ij} = 2\mu\delta_{ijkl} - A|Y|\delta_{ij}\delta_{kl} = 2\mu\delta_{ijkl} - \frac{p_a}{N\phi}\delta_{ij}\delta_{kl},$$

with

$$s^{kl} = \frac{1}{2}\left(y_k \hat{\mathbf{e}}_l + y_l \hat{\mathbf{e}}_k\right),$$

$\hat{\mathbf{e}}_i$ being the i-th canonical vector of $\mathbb{R}^N$.

Equivalently, denoting with $H^1(Y_S)$ and $L^2(Y_S)$ the standard Sobolev spaces, the mixed variational formulation for the microscopic systems (24) reads: Find $\chi^{kl} \in H^1(Y_S), \eta^{kl} \in L^2(Y_S)$, such that

$$\begin{aligned} &\int_{Y_S} \left(2\mu e(\chi^{kl}) : e(v) - \eta^{kl} \operatorname{div}(v)\right) dy + \int_{Y_S} q \ \operatorname{div}(\chi^{kl})\, dy = \\ &\quad - \int_\Gamma T^{kl}\boldsymbol{n} \cdot v \, ds(y) - \int_{Y_S} \delta_{kl} q \, dy. \end{aligned} \tag{25}$$

for all $v \in H^1(Y_S)$ with $v|_\Gamma = 0$ and $q \in L^2(Y_S)$, both Y-periodic functions.

Remark 2.4 *Notice that problem* (24) *describes an incompressible solid for $k \neq l$, and a compressible solid when $k = l$.*

Some algebra on the right hand side of $(24)_3$ yields the following expressions for T^{kl} in two dimensions:

$$T^{11} = \begin{bmatrix} 2\mu - \frac{p_a}{2\phi} & 0 \\ 0 & -\frac{p_a}{2\phi} \end{bmatrix}, \quad T^{12} = T^{21} = \begin{bmatrix} 0 & \mu \\ \mu & 0 \end{bmatrix}, \quad T^{22} = \begin{bmatrix} -\frac{p_a}{2\phi} & 0 \\ 0 & 2\mu - \frac{p_a}{2\phi} \end{bmatrix},$$

while for a three dimensional problem one obtains

$$T^{11} = \begin{bmatrix} 2\mu - \frac{p_a}{3\phi} & 0 & 0 \\ 0 & -\frac{p_a}{3\phi} & 0 \\ 0 & 0 & -\frac{p_a}{3\phi} \end{bmatrix}, \quad T^{12} = T^{21} = \begin{bmatrix} 0 & \mu & 0 \\ \mu & 0 & 0 \\ 0 & 0 & 0 \end{bmatrix},$$

$$T^{22} = \begin{bmatrix} -\frac{p_a}{3\phi} & 0 & 0 \\ 0 & 2\mu - \frac{p_a}{3\phi} & 0 \\ 0 & 0 & -\frac{p_a}{3\phi} \end{bmatrix}, \quad T^{13} = T^{31} = \begin{bmatrix} 0 & 0 & \mu \\ 0 & 0 & 0 \\ \mu & 0 & 0 \end{bmatrix},$$

$$T^{23} = T^{32} = \begin{bmatrix} 0 & 0 & 0 \\ 0 & 0 & \mu \\ 0 & \mu & 0 \end{bmatrix}, \quad T^{33} = \begin{bmatrix} -\frac{p_a}{3\phi} & 0 & 0 \\ 0 & -\frac{p_a}{3\phi} & 0 \\ 0 & 0 & 2\mu - \frac{p_a}{3\phi} \end{bmatrix}.$$

2.1.4 Two-dimensional case

For the sake of simplicity, in what follows we will restrict to the two-dimensional case. Thanks to the symmetry properties of the cell problems, the whole elasticity tensor C^{eff} is uniquely defined by six values:

$$\begin{aligned} a_1 &= C^{eff}_{1111}, \\ a_2 &= C^{eff}_{1212} = C^{eff}_{1221} = C^{eff}_{2112} = C^{eff}_{2121}, \\ a_3 &= C^{eff}_{1122} = C^{eff}_{2211}, \\ a_4 &= C^{eff}_{1121} = C^{eff}_{1211} = C^{eff}_{2111} = C^{eff}_{1112}, \\ a_5 &= C^{eff}_{1222} = C^{eff}_{2122} = C^{eff}_{2212} = C^{eff}_{2221}, \\ a_6 &= C^{eff}_{2222}. \end{aligned} \tag{26}$$

Indeed, since the geometry of the domain is symmetric with respect to the coordinate axes, it can be shown that the only relevant terms are a_1, a_2 and a_3, due to the relations $a_6 = a_1$ and $a_4 = a_5 = 0$ [7]. According to (22), given the local solutions (χ^{kl}, η^{kl}) of (25), the entries of the macroscopic tensor C^{eff} are computed via

$$\begin{aligned} a_1(\mu, p_a, \phi) = C^{eff}_{1111} &= \frac{p_a}{N(1-\phi)} + 2\mu + \underbrace{\frac{1}{1-\phi}\int_{Y_S} \left(-\eta^{11} + 2\mu\partial_x \chi_1^{11}\right)}_{\sigma_{1111}}, \\ a_2(\mu, p_a, \phi) = C^{eff}_{1212} &= \mu + \underbrace{\mu\frac{1}{1-\phi}\int_{Y_S} \left(\partial_y \chi_1^{12} + \partial_x \chi_2^{12}\right)}_{\sigma_{1212}}, \\ a_3(\mu, p_a, \phi) = C^{eff}_{1122} &= \frac{p_a}{N(1-\phi)} + \underbrace{\frac{1}{1-\phi}\int_{Y_S} \left(-\eta^{22} + 2\mu\partial_y \chi_2^{22}\right)}_{\sigma_{1122}}. \end{aligned} \tag{27}$$

It is important to remind that many of the results of the subsection 2.1 has been previously obtained in [7] for compressible and incompressible solid matrices with gaseous bubbles, in the

assumption of a quasi-static regime. Here we have shown that these findings can be straightforwardly extended to a time harmonic regime. In the following part, we will focus on the numerical validation of the homogenized model for quasi-static (or simply called static) regime.

2.2 Numerical validation of two-scale model

The scope of this section is to validate the accuracy properties of the homogeneized elasticity tensor, through a qualitative comparison of the results of a direct numerical simulation at the microscopic level, i.e. solving (4) on a computational mesh which geometrically resolves the microstructure of the material. Let us consider the domain $\Omega = [0, 0.5] \times [0, 0.5]$, and a material with elasticity modulus $\mu = 10^6$ Pa, containing regularly spaced, circular, gaseous inclusions of small radius $r_b = 0.005$, at distance $\Delta x = \Delta y = 0.033$ in x and y directions, respectively. The porosity of the resulting homogenized material is $\phi = \frac{\pi r_b^2}{\Delta x \, \Delta y} = 0.07$.

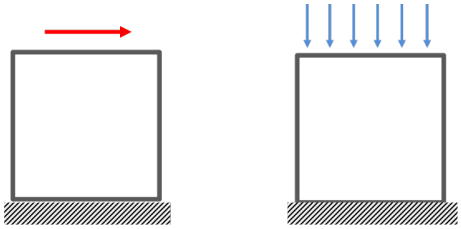

Figure 2: Sketch of the shear test (left) and of the compression test (right).

In order to validate the accuracy properties of the homogenized elasticity tensor 27, we consider two different setups:

- a *shear* problem, imposing a shear on the top boundary (Figure 2, left) and fixing the bottom boundary;
- a *compression* problem, applying a constant force on top of the sample, and fixing the vertical displacement of the bottom boundary (Figure 2, right).

In both cases, gas is at pressure $p_a = 0$ and free stress boundary conditions are imposed on left and right boundaries.

For both configurations, we solve the elasticity problem (4) on a fine mesh, which fully resolves the solid-gas interfaces (125 000 nodes, see Figure 3, left), and on a coarse mesh of the same domain (1500 nodes, Figure 3, right), where the bubbles are not resolved and the material is assumed to be described by the effective effective elasticity tensor, computed through (25) and (27).

A qualitative comparison of the numerical results is shown in Figures 4 and 5. In particular, these demonstrate that the effective tensor computed solving the cell problems (25) for the selected values of μ, p_a and r_b, and using the homogenized model (27), can successfully reproduce the elastic behavior of the material.

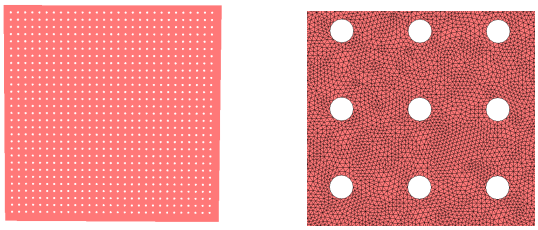

Figure 3: **Left.** The benchmark geometry for testing the homogeneized elasticity tensor. **Right.** Zoom of the computational mesh near the gaseous inlcusions, to highlight the level the resolution of the gas–solid interface.

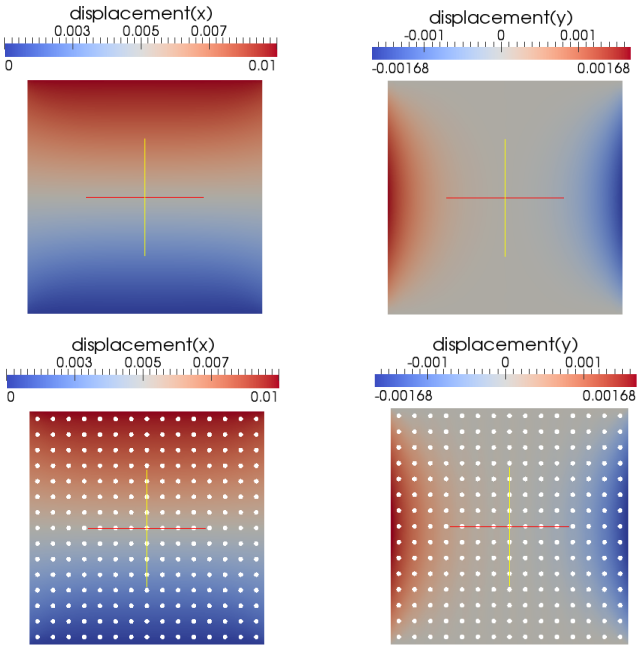

Figure 4: Comparison of homogenized (top) and direct numerical simulations (bottom) for the shear test. **Left.** Displacements in x direction. **Right.** Displacements in y direction.

3 Semi-analytical multiscale model

The two-scale asymptotic model described in Section 2 allows to characterize the elastic material without resolving explicitly the interaction between the incompressible matrix and the gaseous inclusions.

Our ultimate goal is to set up a variational based estimation procedure, which is able to recover the porosity ϕ through an inverse solution of the homogenized problem (19). Hence, since the effective elastic tensor C^{eff} requires the solution of a microscopic cell problem (25) for each configuration of the physical parameters μ, p_a, ϕ, the homogenized model might still result computationally costly.

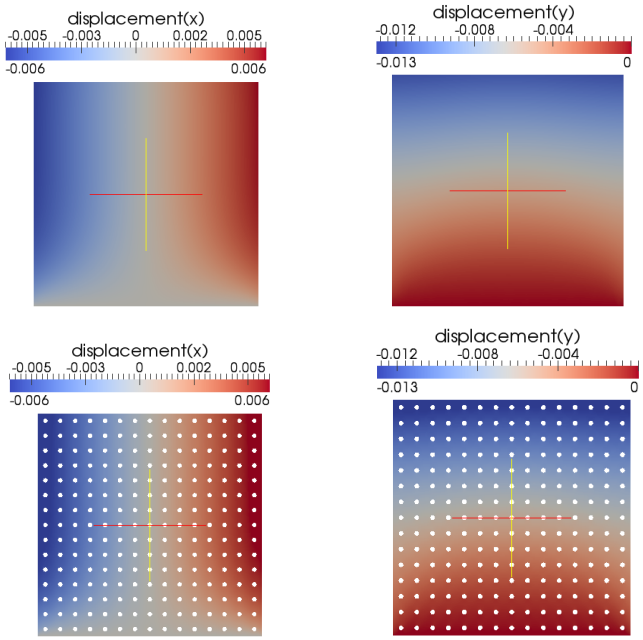

Figure 5: Comparison of homogenized (top) and direct numerical simulations (bottom) for the compression test. **Left.** Displacements in x direction. **Right.** Displacements in y direction.

The scope of this section is to further improve the efficiency of the two-scale model, obtaining approximated *a priori* expression of the averaged local tensors $\sigma_{ijkl} = \langle \sigma_{ij}(\chi^{kl}, \eta^{kl}) \rangle$ and thus of the coefficients a_1, a_2 and a_3 (27), through heuristic and analytical considerations on the cell problems (24). For the sake of simplicity, we restrict to the two-dimensional case ($N = 2$) and assume to deal with circular inclusions.

3.1 Gas pressure

Firstly, we observe that the pressure p_a appears on the diagonal of the tensors T^{kl} for $k, l = 11$ and $k, l = 22$. As a consequence, one can prove that the effect of p_a is a translation of the solution for η^{11} and η^{22} by the constant factor $\frac{p_a}{N\phi}$.

In fact, let us denote by $(\chi_0^{kl}, \eta_0^{kl})$ the solution to (24) for $p_a = 0$ and by by $(\chi_{p_a}^{kl}, \eta_{p_a}^{kl})$ a solution for $p_a \neq 0$. Then $(\delta\chi^{kl}, \delta\eta^{kl}) = (\chi_{p_a}^{kl} - \chi_0^{kl}, \eta_{p_a}^{kl} - \eta_0^{kl})$ must satisfy

$$\begin{cases} -\operatorname{div}_y \sigma_y(\delta\chi^{kl}, \delta\eta^{kl}) &= 0 & \text{in } Y_S, \\ \operatorname{div}_y \delta\chi^{kl} &= 0 & \text{in } Y_S, \\ \sigma_y(\delta\chi^{kl}, \delta\eta^{kl} + p_a/(N\phi))\boldsymbol{n} &= \mathbf{0} & \text{on } \Gamma, \\ \chi^{kl}, \eta^{kl} & \text{are } Y - \text{periodic.} \end{cases} \tag{28}$$

Assuming that $\int_{Y_S} \chi_0^{kl}(y)\, dy = \int_{Y_S} \chi_{p_a}^{kl}(y)\, dy = 0$, to remove the constant from the periodic boundary conditions, the above problem (28) has only the solution $(\frac{p_a}{N\phi}, 0)$, i.e. $\eta_{p_a}^{kl} = \eta_0^{kl} + p_a/(N\phi)$ and $\chi_{p_a}^{kl} = \chi_0^{kl}$.

Therefore, since the average of η^{kl} enters into the formulas for σ_{ijkl}, we have:

$$\sigma_{1111}(\mu, p_a, \phi(r)) = \sigma_{1111}(\mu, 0, \phi(r)) + \frac{p_a}{N\phi}\,,$$

$$\sigma_{1122}(\mu, p_a, \phi(r)) = \sigma_{1122}(\mu, 0, \phi(r)) + \frac{p_a}{N\phi}\,.$$

On the other hand, σ_{1212} does not depend on p_a.

This implies that the tensor obtained in (22) must take the form

$$C^{eff}_{ijkl} = \frac{p_a}{N\phi(1-\phi)}\delta_{ij}\delta_{kl} + 2\mu\delta_{ijkl} + \langle\left[\sigma_y(\chi^{kl}, \eta^{kl})\right]_{ij}\rangle_{Y_s}\Big|_{p_a=0}\,.$$

3.2 Shear modulus

The considerations in Section 3.1 allows to restrict, without loss of generality, to the case $p_a = 0$. In this case, the tensors T^{kl} are linear in μ. This allows to rewrite the equations for the microscopic cell problems (24) in terms of the variables

$$(\chi^{kl}, \hat{\eta}^{kl}) = (\chi^{kl}, \frac{1}{\mu}\eta^{kl})$$

yielding equations which are independent from the elasticity modulus. One can conclude that χ^{kl} is independent from μ, while η^{kl} is linear in μ. Hence, the averaged tensors can be written as

$$\begin{aligned}
\sigma_{1111}(\mu, p_a, \phi(r)) &= \mu\,\underbrace{\sigma_{1111}(1, 0, \phi(r))}_{\alpha_1(\phi)} + \frac{p_a}{N\phi}\,,\\
\sigma_{1212}(\mu, \phi(r)) &= \mu\,\underbrace{\sigma_{1212}(1, \phi(r))}_{\alpha_2(\phi)}\,,\\
\sigma_{1122}(\mu, p_a, \phi(r)) &= \mu\,\underbrace{\sigma_{1122}(1, 0, \phi(r))}_{\alpha_3(\phi)} + \frac{p_a}{N\phi}\,.
\end{aligned} \tag{29}$$

Therefore, the computation of the entries of C^{eff} is reduced to the computation of the functions $\alpha_1(\phi)$, $\alpha_2(\phi)$, $\alpha_3(\phi)$. i.e. the solution to the cell problems (25) for $\mu = 1$ and $p_a = 0$, and that only depend on the porosity ϕ.

Remark 3.1 (Effective Lamé coefficients) *Using this result, and taking into account the contribution of p_a, the tensor takes the form*

$$C^{eff}_{ijkl} = \frac{p_a}{N\phi(1-\phi)}\delta_{ij}\delta_{kl} + 2\mu\delta_{ijkl} + \mu\langle\left[\sigma_y(\chi^{kl}, \eta^{kl})\right]_{ij}\rangle_{Y_s}\Big|_{p_a=0,\mu=1}\,.$$

If the microstructure term could be factorized as

$$\langle\left[\sigma_y(\chi^{kl}, \eta^{kl})\right]_{ij}\rangle_{Y_s}\Big|_{p_a=0,\mu=1} = a\delta_{ij}\delta_{kl} + 2b\delta_{ijkl},$$

Then, we could now retrieve the contributions of the microstructure to each of the Lamé parameters: $\lambda^{eff} = \frac{p_a}{N\phi(1-\phi)} + \mu a,$, $\mu^{eff} = \mu(1+b)$. *However, it is not clear how the microstructure term directly affects both Lamé coefficients, because it can vary with the microgeometry of* Y_S *and analytic expressions for* χ *and* η *are not available.*

3.3 Porosity

3.3.1 The incompressible cell problem (12)

The function

$$\alpha_2(\phi) = \frac{1}{1-\phi} \int_{Y_S} \left(\partial_y \chi_1^{12} + \partial_x \chi_2^{12} \right)$$

depends on χ^{12}, which can be seen as the solution of a Stokes-like problem (where χ^{12}, η^{12} will represent the velocity and the pressure, respectively) with a prescribed shear stress on the gaseous inclusion boundary.

A first approximation of α_2 can be based on the following considerations. In the case $\phi = 0$, α_2 corresponds to the shear elastic coefficient of an incompressible solid without any gaseous inclusion, i.e. $\alpha_2(0) = \mu = 1$. Moreover, we assume that when ϕ achieves its maximum value, we must have $\alpha_2 = 0$. This maximum value of ϕ depends on the shape of the inclusion. For a circular inclusion we have $\phi_{\max} = \frac{\pi}{4}$ (when the diameter is equal to 1), yielding

$$\alpha_2(\phi) \approx \left(1 - \frac{4}{\pi}\phi\right) . \tag{30}$$

3.3.2 The compressible cell problems (11) and (22)

The coefficient α_1 has the form

$$\alpha_1(\phi) = \frac{1}{1-\phi} \int_{Y_S} (-\hat{\eta}_{11} + 2\partial_{y_1} \chi_{11,y_1}) = \langle \hat{\eta}_{11} \rangle + 2\langle \partial_{y_1} \chi_{11,y_1} \rangle .$$

The first term corresponds to the value of the pressure over the microscopic cell, when a given stress (both normal and tangential) is applied at the interface Γ. Notice that the boundary stress is defined by μ and p_a only, and does not depend on the porosity. On the other hand, for lower porosity, the amount of compressible volume decreases, inversely proportional to the fluid volume Y_F. Hence, for the pressure term $\langle \eta_{11} \rangle$, which is strictly related to the normal compression efforts inside the solid, we use the ansatz of the form

$$\langle \hat{\eta}_{11} \rangle \approx \frac{\kappa}{\phi}, \tag{31}$$

for a parameter $\kappa > 1$. Based on a numerical evidence, we set $\kappa = 1$ (as it will be shown through the validation in Section 3.4).

Concerning the second contribution, notice that, for $\phi \to 0$ (an elastic material without gaseous inclusion), we have

$$\operatorname{div} \chi^{11} = -1$$

(constant over Y) and, since $\chi_1^{11} = \chi_2^{11}$ (by symmetry), one can conclude

$$\partial_{y_1} \chi_1^{11}|_{\phi \to 0} = -\frac{1}{2}\,. \tag{32}$$

At the same time, we observe that in the range of low to medium porosity, the term $\partial_{y_1}\chi_{11,y_1}$ has only a secondary effect on the tensor coefficient, with respect to the term (31). As a consequence, we use the constant value (32) as an approximation of the divergence of χ over the whole solid domain, i.e.

$$\langle \partial_{y_1} \chi_1^{11} \rangle \approx -\frac{1}{2}\,, \tag{33}$$

which yields

$$\alpha_1(\phi) \approx \frac{1}{\phi} - 1\,. \tag{34}$$

Finally, in the case of circular inclusions, based on the symmetry properties of the cell problem (24) one can conclude that $\langle \sigma_{1111} \rangle = \langle \sigma_{1122} \rangle$, i.e. $\alpha_3(\phi) = \alpha_1(\phi)$.

3.4 Approximated expressions for tensor coefficients

Using the above approximations (30) and (34), we can write the effective tensor coefficients as

$$\begin{aligned} a_1(\mu, p_a, \phi(r)) &\approx \frac{p_a}{N(1-\phi)} + 2\mu + \frac{p_a}{N\phi} + \frac{\mu}{\phi} - \frac{2\mu}{1-\phi}\frac{1-\phi}{2} = \\ &= \frac{p_a}{N}\frac{1}{\phi(1-\phi)} + \frac{\mu}{\phi} + \mu \\ a_2 &\approx \mu\left(1 - \frac{4}{\pi}\phi\right) \\ a_3 &\approx \frac{p_a}{N}\frac{1}{\phi(1-\phi)} + \frac{\mu}{\phi} - \mu\,. \end{aligned} \tag{35}$$

We tested numerically the validity of expressions (35) over a wide range of values of p_a, μ and ϕ (in the case circular inclusions). Figure 6 compares the analytical expressions for the coefficients $\alpha_i(\phi)$ ($i = 1, 2, 3$) against the numerical results, while in Figure 7 we show the results for a fixed value of $\mu = 10^6$ of the tensor coefficients a_1 and a_2 for a wide range of pressure and porosity. In both cases, we obtain an excellent qualitative agreement. A quantitative comparison is provided in Figure 8, depicting the level curves of the relative error between the expressions (35) and the numerical results. Focusing on low porosities (below 0.25), for the coefficient a_1 we obtain a maximum error of less than 20% for $\mu = 10^6$, decreasing down to 7% when $\mu = 10^7$. We obtained similar results for a_3 (not shown), while for a_2, which is linear in μ and independent from pressure, the relative error stays below 4% (for $\phi < 0.25$).

4 Application to an inverse problems for porosity estimation

In this section, we exploit the homogenization theory described in Section 2 and the analytical approximations for the effective tensor coefficients derived in Section 3, to define a two-scales

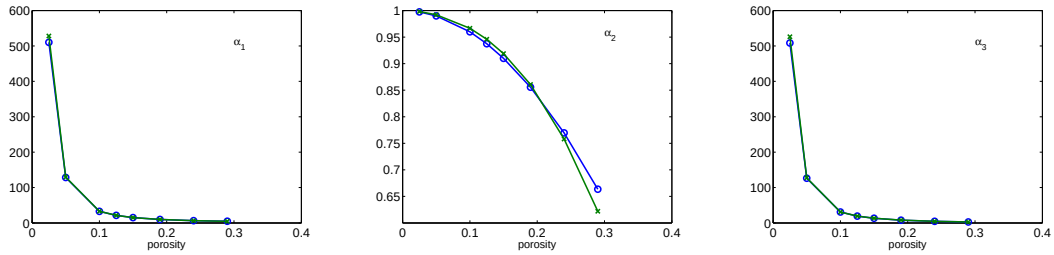

Figure 6: Comparisons between the numerical results for $\alpha_i(\phi)$ ($i = 1, 2, 3$, green) and the semi-analitical expression (30)-(34) (blue), as a function of ϕ.

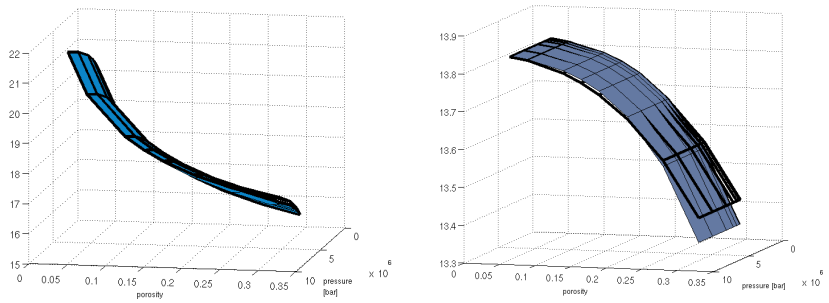

Figure 7: Left: Surface plot of the coefficient a_1 for $\mu = 10^6$ Pa (in logarithmic scale) versus pressure and porosity (light blue) superimposed to the analytical expression (35) (bold). Right: Surface plot of the coefficient a_2 for $\mu = 10^6$ Pa (in logarithmic scale) versus pressure and porosity (light blue) superimposed to the analytical expression (35) (bold).

variational-based estimation algorithm for the identification of material porosity using harmonic wave analysis, without resolving numerically the dynamics of gaseous inclusions at the fine scale.

4.1 Problem setting

As in Section 2, let us consider an elastic material, composed of an incompressible elastic matrix with a known elasticity modulus μ, and small gaseous inclusions at a given pressure p_a. We assume that the available data describe a set of measurements

$$\mathbf{d}^{\omega}_{\text{exp}} : \mathcal{M} \to \mathbb{R}^d$$

of the internal displacement field in a subdmoain $M \subset \Omega$, in response to an excitation at frequency ω. Typically, $\mathcal{M}$ will consist of a finite set of points of Ω (e.g. a Cartesian lattice). This assumption describes the outcome of a set of MRE experiments, in which shear and/or compression waves at a given frequency ω are applied on the boundary of the sample, and MRI is used to recover the inner displacement field at selected points. For the sake of simplicity, we will consider that the measures $\mathbf{d}^{\omega}_{\text{exp}}$ are available on the whole domain Ω, implicitly assuming that, if this is not the case, a proper interpolation can be used.

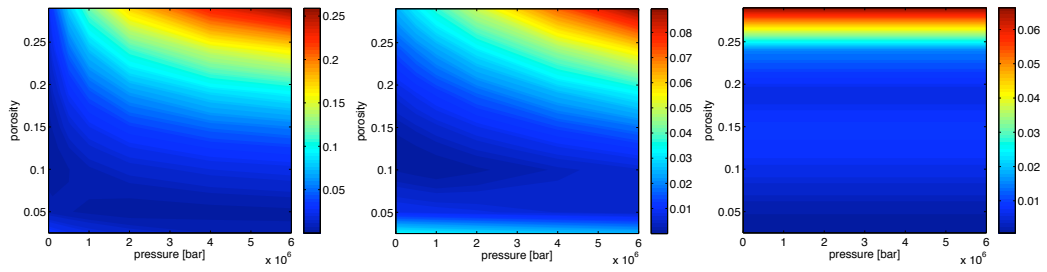

Figure 8: Validation of semi-analytical expressions (35). Left: Error in the coefficient a_1 for $\mu = 10^6$ Pa. Center. Error in the coefficient a_1 for $\mu = 10^7$ Pa. Right. Error in the coefficient a_2 for $\mu = 10^6$ Pa.

4.2 Variational approach

In what follows, we assume that the porosity field $\phi(\boldsymbol{x}) : \Omega \to [0, 1]$ is the only unknown parameter. Hence, we can write the inverse problem as a minimization problem for a functional

$$J(\phi) = \int_\Omega (\mathbf{d}_\phi - \mathbf{d}^\omega_{\text{exp}})^2 \,, \tag{36}$$

where $\mathbf{d}_\phi$ denotes the numerical solution for the macroscopic displacement, corresponding to a particular porosity field ϕ:

$$\begin{cases} -\overline{\rho}\omega^2 \mathbf{d}_\phi - \text{div}\left(C^{eff} e_x(\mathbf{d}_\phi)\right) = 0, \text{ in } \Omega, \\ C^{eff} e_x(\mathbf{d}_\phi)\boldsymbol{n} = 0 \text{ on } \Gamma_N, \\ \mathbf{d}_\phi \cdot \boldsymbol{n} = \mathbf{d}_{\text{bd}} \text{ on } \Gamma_D. \end{cases} \tag{37}$$

We solve the minimization problem for $J(\phi)$ using a variational approach, with a procedure similar to the one described in [12, 13]. To this aim, we first compute the derivative of $J(\phi)$ with respect to a given increment θ of the the porosity field

$$\langle \frac{\partial J}{\partial \phi}, \theta \rangle = 2 \int_\Omega \left((\mathbf{d}_\phi - \mathbf{d}^\omega_{\text{exp}}) \cdot \partial_\phi \mathbf{d}_\phi \right) \theta \, dx. \tag{38}$$

Then, in order to define a suitable descent direction, we introduce the adjoint problem

$$\begin{cases} -\overline{\rho}\omega^2 \mathbf{z}_\phi - \text{div}\left(C^{eff} e_x(\mathbf{z}_\phi)\right) = \mathbf{d}_\phi - \mathbf{d}^\omega_{\text{exp}} & \text{in } \Omega, \\ \mathbf{z}_\phi = 0 & \text{on } \Gamma_N, \\ \mathbf{z}_\phi \cdot \boldsymbol{n} = 0 & \text{on } \Gamma_D. \end{cases} \tag{39}$$

which allows to rewrite equation (38) as

$$\langle \frac{\partial J}{\partial \phi}, \theta \rangle = 2 \int_\Omega \left(\omega^2(\rho_f - \rho_s)(\mathbf{d}_\phi - \mathbf{z}_\phi) - \left[\partial_\phi C^{eff}\right] e(\mathbf{d}_\phi) : e(\mathbf{z}_\phi) \right) \theta \, dx.$$

Hence, a descent direction for J is obtained defining

$$\theta = -\alpha S,$$

where $\alpha > 0$ is a free parameter, to be chosen to control the length of the step along the θ-direction and

$$S = \omega^2(\rho_f - \rho_s)(\mathbf{d}_\phi - \mathbf{z}_\phi) - \left[\partial_\phi C^{eff}\right] e(\mathbf{d}_\phi) : e(\mathbf{z}_\phi). \tag{40}$$

Thanks to the results of Section 3, the tensor $\partial_\phi C^{eff}$ in (40), i.e. the derivative of C^{eff} with respect to ϕ, can be computed analitically using the approximations (35). Without these approximations, one would have to perform a large amount of numerical evaluation for different bubble sizes, in order to obtain a reliable finite difference approximation for each tensorial component.

Our two-scale estimation algorithm can be summarized as follows.

Algorithm (porosity estimation). Let be given an initial condition $\phi^{(0)} = \phi_0$. Set $\alpha^{(0)} = 1$ and evaluate $S^{(0)} = S(\phi^{(0)})$ as in (40). For $k > 0$, let be be given $\phi^{(k)}, \alpha^{(k)}$ and a descent direction $S^{(k)}$. Until convergence, do:

1 Compute $\phi^{(k)} = \phi^{(k-1)} - \alpha^{(k)} S^{(k)}$ (restrict ϕ between 0 and 1)

2 Evaluate the homogeneized tensor $C^{eff}(\phi^{(k)})$ from (35)

3 Solve (37) and compute the macroscopic solution $\mathbf{d}^{(k)}$

4 Evaluate $J^{(k)} = J(\phi^{(k)})$

- if $J^{(k)} \geq J^{(k-1)} \Rightarrow$ set $\phi^{(k+1)} = \phi^{(k)}$, $\alpha^{(k+1)} = \frac{\alpha^{(k)}}{2}$ and go back to step 1
- else (if $J^{(k)} < J^{(k-1)}$)

5 Evaluate the derivatives of $C^{eff}(\phi^{(k)})$

6 Solve the adjoint problem (39) for $\mathbf{z}^{(k)}$

7 Compute $S^{(k)}$ using (40)

Different stopping criteria might be used. In the numerical results presented below, we used either the magnitude of the step $\alpha^{(k)}$ or the relative decrease of $J(\phi)$ between successive iterations as indicators of convergence.

4.3 Numerical results

4.3.1 Validation: estimation of homogenized porosity

In this first test, we apply the estimation algorithm to recover the porosity field of a homogenized material. Namely, let us consider a weakly compressible elastic material in the domain $\Omega = [0, 1.2] \times [0, 1.2]$, with a porosity of $\phi_{out} = 0.05$, except in two disjoint inner subdomain with porosity of $\phi_{in} = 0.1$ (Figure 9, left).

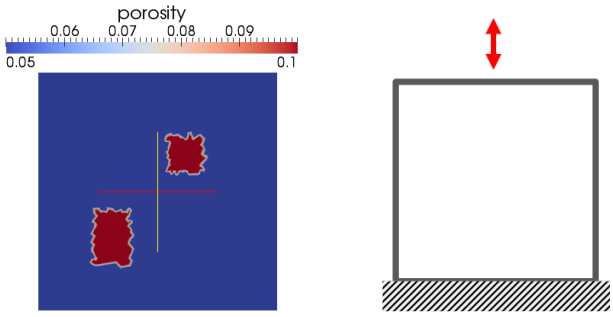

Figure 9: **Left.** Exact porosity field for the homogenized benchmark. **Right.** Sketch of the considered experiment, where a compression wave is imposed through a harmonic boundary displacement.

The field $\mathbf{d}_{\text{exp}}$ consists of synthetic data, generated running a *forward* simulation using the two-scale homogenized model (Sections 2–3) on a computational mesh of about 10.000 nodes. Additionally, these results have been perturbed adding noise of different intensities, i.e. by considering $\mathbf{d}_{\text{exp}}(1 + \frac{I}{2}\xi)$, where I denotes the intensity of the noise and ξ is a random variable uniformly distributed in $[-1, 1]$. We considered a compression test (Figure 9, right), where a harmonic displacement with frequency $\nu = 50\,\text{Hz}$ and amplitude $\mathbf{d}_{\text{top}} = 0.02$ m is imposed on top of the sample.

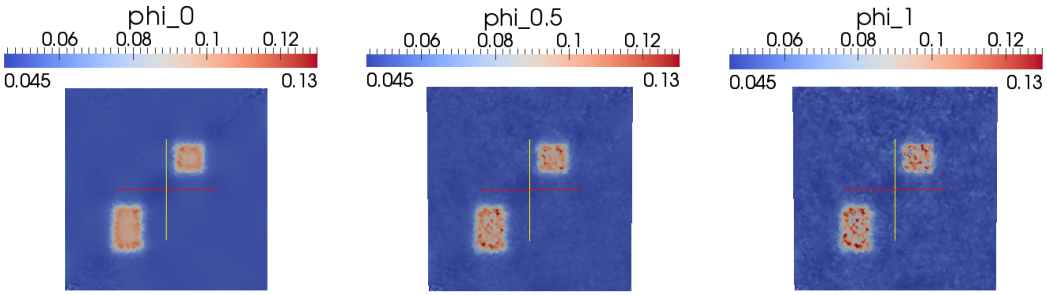

Figure 10: Result of the estimation algorithm, using the reference solution as measurement field. From left to right: no noise, noise intensity 0.5%, noise intensity 1%.

The estimation algorithm is then applied, in order to minimize $J(\phi)$ based on the same homogenized problem. Figure 10 shows the contour lines of the porosity field for three different intensities of noise, while Figure 11 depicts the porosity fields along the diagonal, increasing the intensity of the noise.

4.3.2 Multiscale estimation test

Finally, we use the porosity estimation algorithm within a multiscale framework, addressing the estimation of the material porosity from a set of synthetic data obtained from a direct numerical simulation at the microscale level.

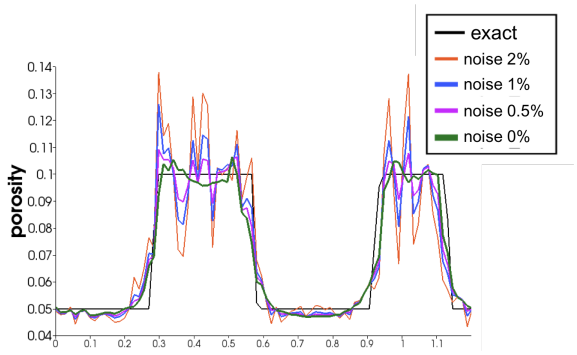

Figure 11: Cross section of the porosity fields along the diagonal, for different noise intensities on the reference measurements, compared with the exact solution (in black).

Let us consider an elastic and incompressible material with shear modulus $\mu = 10^6$ Pa and environmental pressure $p_a = 0$ Pa in the domain $\Omega = [0, 0.66] \times [0, 0.66]$ with

$$\phi(\boldsymbol{x}) = \begin{cases} 0.1 & \text{if } \boldsymbol{x} \in \hat{\Omega} = [0.2, 0.4] \times [0.3, 0.5] \\ 0.045 & \text{if } \boldsymbol{x} \in \Omega \setminus \hat{\Omega}, \end{cases}$$

as shown in Figure 12, left. This time, in order to simulate the solid–gas interfaces in a more realistic situation, the synthetic data were generated by performing the numerical simulation of the elastic and incompressible problem (4) with embedded bubbles on a very fine grid (around 130.000 nodes). As next, these results have been interpolated on a much coarser grid and perturbed adding noise fields of varying intensity.

To analyze the sensitivity with respect to the mesh size, we have tested the simulations in two different macroscopic meshes, composed by 2000 and 6000 nodes, respectively. The results of the estimation, without adding noise to synthetic data, are shown in Figure 12 for the stationary and for the harmonic regime. In both cases, the algorithm can successfully detect the inhomogenities, and it is not very sensitive to the mesh size, yielding only a slight improvement using a finer mesh. We also observe the arise of small additional oscillations in the non-stationary case, which, however, do not seem to affect substantially the quality of the final result.

Remark 4.1 (Miscroscopic synthetic data) *It is worth stressing that in the previous Section 4.3 we used the numerical solution of the homogenized model as reference solution for the minimization of the functional $J(\phi)$, which is computed using the same homogenized approximation. Hence, the exact solution corresponds indeed to a minimum of the functional. Now, to mimic a realistic measurement process, the synthetic data have been taken from a microscale simulation, which is connected to the inversion algorithm only through the two-scale approximation for the effective tensor coefficients. Therefore, this first computation – with unperturbed synthetic data – serves also as intrinsic validation of the accuracy properties of the homogenized model.*

As next, we focus on the coarse grid and on the time-harmonic excitation, investigating the effect on the results of perturbing the synthetic data with increasing noise intensities, up to 20%. From

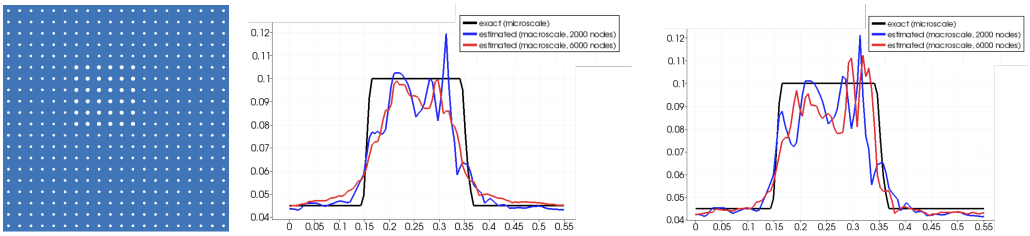

Figure 12: **Left.** The microscale geometry used for testing the multiscale estimation algorithm. **Center.** Estimated values of the porosity along the centerline of the sample in the stationary case (frequency $\nu = 0$). In black, the value of the porosity computed from the microscale structure (shown on the left). In blue and red , the estimated porosity through the two-scale homogenization and the estimation algorithm, using a mesh with 2000 nodes and a finer mesh with 6000, respectively. **Right.** Results in the harmonic regime (50 Hz).

the point of view of application, this test is particularly relevant, as imaged displacement field are often characterized by a high level of noise. The results for the porosity profiles along a horizontal cross-section are depicted in Figure 13. We observe that up to 10% of noise the estimation algorithm is still able to locate the higher porosity subdomain. Only for larger perturbation the results become inaccurate, although one can still see a global increase in the porosity in the overall domain (not shown).

As a final remark, notice that all the computations needed for estimation procedure are based only on the macroscopic mesh (homogenized model), and the microscopic results are upscaled on this coarse level. In our simulations, solving the direct problem based on the homogenized model (i.e. a simpler elasticity equation on a much coarser mesh) allowed a speed-up of about 99% for each forward iteration. Nevertheless, as a final result we are able to retrieve satisfactory information on the microscale structure.

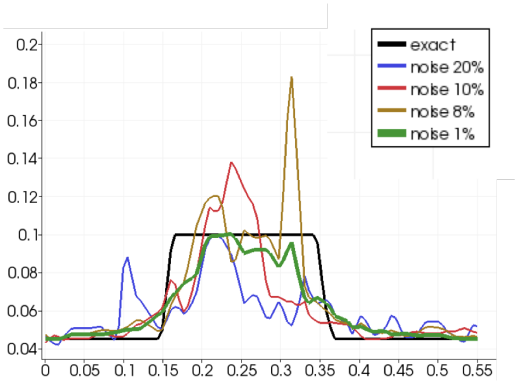

Figure 13: Plot of the estimated porosity over a horizontal cross section ($y = 0.4$), perturbing the reference data with noise of increasing intensity (up to 25%). Simulations on a computational mesh of 2000 nodes.

5 Conclusions

This paper discusses the inverse problem of estimating the porosity of a compressible material composed of an incompressible elastic matrix and small gaseous inclusions. In particular, we decoupled two spatial scales of the problem (the macroscopic scale of the compressible effective material and the microscopic scale of the gaseous inclusions) based on a recently proposed the two-scale homogenization [7]. First, we obtained a homogenized model for the effective compressible material in harmonic regime, validating numerically the theoretical findings via a comparison of the homogenized model with direct numerical simulations. As next, we derived semi-analytical expressions for the effective elastic tensor coefficients, which allow to simulate the macroscale behavior without the need of performing numerical simulations at the microscale of the gaseous inclusions. This results have been used to define an efficient variational based inversion algorithm. One of the main achievements of this multiscale inversion approach is that we are able to characterize the microstructure (bubble size) using much less computational resources (up to 99% less computational time), compared with the full solutions and evaluations on the fine – microscopic – mesh.

Acknowledgements

This work has been funded by the joint DFG-CONICYT grant CA-1159/1, for *Initiation and intensification of bilateral cooperations*. The Authors wish to thank Prof. Dr. I. Sack and Dr. S. Hirsch (MRE research group, *Charité*, Berlin) for the useful discussions. The numerical simulations have been performed using the open source software FreeFem++ [23].

References

[1] MANZONI A., A. QUARTERONI, AND G. ROZZA, *Model reduction techinques for fast blood flow simulation in parametrized geometries*, Int. J. Numer. Meth. Biomed. Engnr., 28 (2012), pp. 604–625.

[2] ——, *Shape optimization for viscous flows by reduced basis methods and free-form deformation*, Int. J. Numer. Meth. Fluids, 70 (2012), pp. 646–670.

[3] U. ALBOCHER, A.A. OBERAI, P.E. BARBONE, AND I. HARARI, *Adjoint-weighted equation for inverse problems of incompressible plane-stress elasticity*, Comp. Meth. Appl. Mech. Engnr., 198 (2009), pp. 2412–2470.

[4] G. ALLAIRE, *Homogenization of the Navier-Stokes equations in open sets perforated with tiny holes. I. Abstract framework, a volume distribution of holes*, Arch. Rational Mech. Anal., 113 (1990), pp. 209–259.

[5] ——, *Homogenization and two-scale convergence*, SIAM J. Math. Anal., 23 (1992), pp. 1482–1518.

[6] A. ÁVILA, G. GRISO, B. MIARA, AND E. ROHAN, *Multiscale modeling of elastic waves: theoretical justification and numerical simulation of band gaps*, SIAM Multiscale Modeling ans Simulation, 7 (2008), pp. 1–21.

[7] L. BAFFICO, C. GRANDMONT, Y. MADAY, AND A. OSSES, *Homogenization of elastic media with gaseous inclusions*, SIAM Multiscale Modeling ans Simulation, 7 (2008), pp. 432–465.

[8] M. BOULAKIA, E. SCHENONE, AND J-F. GERBEAU, *Reduced-order modeling for cardiac electrophysiology. Application to parameter identification*, International Journal for Numerical Methods in Biomedical Engineering, 28 (2012), pp. 727–744.

[9] P.G. CIARLET AND J.-L. LIONS, eds., *Handbook of Numerical Analysis, Vol. 2, Finite Element Methods (Part 1)*, North-Holland, 1991.

[10] D. CIORANESCU AND A. PIATNITSKI, *Homogenization in perforated domains with rapidly pulsing perforations*, ESAIM Control Optim. Calc. Var., 9 (2003), pp. 461–483.

[11] F.B. FREIMANN, K.-J. STREITBERGER, D. KLATT, K. LIN, J. MCLAUGHLIN, J. BRAUN, C. SPRUNG, AND I. SACK, *Alteration of brain viscoelasticity after shunt treatment in normal pressure hydrocephalus*, Neuroradiology, 54 (2012), pp. 189–196.

[12] J. GUTIÉRREZ, S.AND MURA, *Small amplitude homogenization applied toinverse problems*, Comp. Mech., 41 (2008), pp. 699–706.

[13] S. GUTIÉRREZ AND J. MURA, *An adaptive procedure for inverse problems in elasticity*, Comptes Rendus Mécanique, 338 (2010), pp. 402–411.

[14] S. HIRSCH, O. POSNANSKY, T. ELGETI, J. BRAUN, AND I. SACK, *Measurement of vibration-induced volumetric strain in the human lung*, Mag. Reson. Med. (in press), (2012).

[15] R. LEIDERMAN, P.E. BARBONE, A.A. OBERAI, AND J.C. BAMBER, *Coupling between elastic strain and interstitial fluid flow: ramifications for poroelasticity imaging*, Phys. Med. Biol., 51 (2006), pp. 6291–6313.

[16] R. LEIDERMAN, A.A. OBERAI, AND BARBONE P.E., *Theory of reconstructing the spatial distribution of the filtration coefficient in vascularized soft tissues: exact and approximate inverse solutions*, Comptes Rendus Mecanique, 338 (2010), pp. 412–423.

[17] M.I. MIGA, *A new approach to elastography using mutual information and finite elements*, Phys. Med. Biol., 48 (2003), pp. 467–480.

[18] P. MOIREAU AND D. CHAPELLE, *Reduced-order Unscented Kalman Filtering with application to parameter identification in large-dimensional systems*, Esaim Contr. Opt. Calc. Var., 17 (2011), pp. 380–405. doi:10.1051/cocv/2010006.

[19] R. MUTHUPILLAI AND R.L. EHMAN, *Magnetic resonance elastography*, Nat. Med., 2 (1996), pp. 601–603.

[20] P.R. PERRIÑEZ, F.E. KENNEDY, E.E.W. VAN HOUTEN, J.B. WEAVER, AND K.D. PAULSEN, *Modeling of soft poroelastic tissue in time-harmonic mr elastography*, IEEE Trans. Biomed. Eng., 56 (2009), pp. 598–608.

[21] A.A. OBERAI, N.H. GOKHALE, M.M. DOYLEY, AND J.C. BAMBER, *Evaluation of the adjoint equation-based algorithm for elasticity imaging*, Inverse Problems, 49 (2004), pp. 2955–2974.

[22] A.A. OBERAI, N.H. GOKHALE, AND G. FEIJOO, *Solution of inverse problems in elasticity imaging using the adjoint method*, Inverse Problems, 19 (2003), pp. 297–313.

[23] O. PIRONNEAU, F. HECHT, AND J. MORICE, *Freefem++, www.freefem.org*.

[24] J. RAHMOUN, F. CHAARI, E. MARKIEWICZ, AND P. DRAZETIC, *Micromechanical modeling of the anisotropy of elastic biological composites*, SIAM Multiscale Modeling ans Simulation, 8 (2009), pp. 326–336.

[25] I. SACK, B. BEIERBACH, U. HAMHABER, D. KLATT, AND J. BRAUN, *Non-invasive measurement of brain viscoelasticity using magnetic resonance elastography*, NMR Biomed, 21 (2008), pp. 265–271.

[26] E. SANCHEZ-PALENCIA, *Non-homogenous media and vibration theory*, Springer-Verlag, 1980.

[27] E. SANCHEZ-PALENCIA AND A. ZAOUI, *Homogenization techniques for composite media*, vol. 272 of Lecture Notes in Physics, Springer-Verlag, 1987.

[28] L. TARTAR, *H-measures, a new approach for studying homogenisation, oscillations and concentration effects in partial differential equations*, Proc. of the Royal Soc. Edinburgh, (1990), pp. 193–230.

[29] J. WUERFEL, F. PAUL, B. BEIERBACH, U. HAMHABER, D. KLATT, S. PAPAZOGLOU, F. ZIPP, P. MARTUS, J. BRAUN, AND I. SACK, *MR-elastography reveals degradation of tissue integrity in multiple sclerosis*, Neuroimage, 49 (2010), pp. 2520–2525.